Fluidizable Ni/La$_2$O$_3$-γAl$_2$O$_3$ catalyst for steam gasification of a cellulosic biomass surrogate

Jahirul Mazumder, Hugo de Lasa*

Chemical Reactor Engineering Centre, Department of Chemical and Biochemical Engineering, The University of Western Ontario, London, ON, Canada N6A 5B9

ABSTRACT

This study reports a new fluidizable Ni catalyst supported on La$_2$O$_3$ modified γ-Al$_2$O$_3$. The 20% Ni/5% La$_2$O$_3$-γAl$_2$O$_3$ catalyst is prepared using a specially designed multistep incipient wetness technique and direct reduction of metal nitrate precursors. Steam gasification of glucose (a biomass surrogate), is developed in a CREC Riser Simulator using the new fluidizable catalyst. Experiments are performed at different steam/biomass ratios, temperatures and reaction times. Catalytic gasification runs confirm the high performance of the Ni/La$_2$O$_3$-γAl$_2$O$_3$ in terms of reforming activity, and reduced coke formation. Furthermore, observed gasification products (H$_2$, CO, CO$_2$, and CH$_4$) are in agreement with thermodynamics, with product yields approaching chemical equilibrium as the reaction time is increased. Furthermore, the value of the Ni/La$_2$O$_3$-γAl$_2$O$_3$ catalyst is demonstrated while comparing its improved performance with respect to the one of other prepared catalysts: (i) an unpromoted Ni/γAl$_2$O$_3$ and (ii) a Ni/La$_2$O$_3$-γAl$_2$O$_3$ prepared via metal precursor calcination. Prepared catalysts are also characterized using BET surface area analysis, TPR, TPO, H$_2$-pulse chemisorption, pyridine FTIR, CO$_2$ and NH$_3$ TPD. It is shown that the addition of lanthanum oxides reduces surface area losses, increasing the thermal stability of γ-Al$_2$O$_3$. La$_2$O$_3$ also improves reducibility and dispersion of the active phase by decreasing nickel-aluminate formation. Pyridine FTIR confirms the absence of Brønsted acid sites in γ-Al$_2$O$_3$, with La$_2$O$_3$ reducing Lewis acidity. Multiple TPO and TPR experiments also show that the prepared catalyst remains stable under repeated oxidation and reduction cycles. As a result, it is proven that the enhanced gasification activity of the Ni/La$_2$O$_3$-γAl$_2$O$_3$ fluidizable catalyst of the present study is in line with their various and favorable structural properties (available Ni surface area and basicity/acidity ratio) modifications.
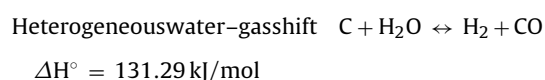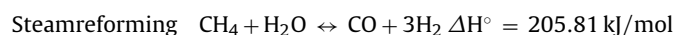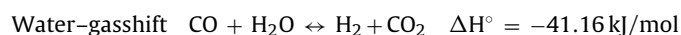
1. Introduction

The use of biomass not only opens a window of a clean, renewable and CO$_2$ neutral energy source but also minimizes the use of fossil fuels and alleviates global warming problems. Gasification technology is able to convert low value and highly distributed solid biomass effectively and economically to a relatively uniform synthesis gas. In recent years, biomass steam gasification has become an area of growing interest because it can produce synthesis gas with a relatively higher hydrogen content [1–5].

Steam gasification of biomass involves a complex network of heterogeneous reactions. One can envision biomass gasification as a combination of primary and secondary reactions [2–6]. *Primary* reactions break down the vaporized biomass molecules, forming permanent gases, higher hydrocarbons, tars and coke. *Secondary* reactions crack or/and reform the higher hydrocarbons and tars into lighter hydrocarbons and permanent gases (CO, CO$_2$, H$_2$). Furthermore, light hydrocarbons, CO and H$_2$ can react with steam and CO$_2$ altering the gas composition with this depending on gasifier conditions as indicated below:

Water–gasshift $CO + H_2O \leftrightarrow H_2 + CO_2$ $\Delta H^\circ = -41.16\,\text{kJ/mol}$

Steamreforming $CH_4 + H_2O \leftrightarrow CO + 3H_2$ $\Delta H^\circ = 205.81\,\text{kJ/mol}$

Dryreforming $CH_4 + CO_2 \leftrightarrow 2CO + 2H_2$ $\Delta H^\circ = 246.98\,\text{kJ/mol}$

Heterogeneouswater–gasshift $C + H_2O \leftrightarrow H_2 + CO$

$\Delta H^\circ = 131.29\,\text{kJ/mol}$

* Corresponding author. Tel.: +1 519 661 2144; fax: +1 519 850 2931.
E-mail address: hdelasa@eng.uwo.ca (H. de Lasa).

Boudouard reaction $C + CO_2 \leftrightarrow 2CO$ $\Delta H^\circ = 172.46\,kJ/mol$

Hydrogenating gasification $C + 2H_2 \leftrightarrow CH_4$

$\Delta H^\circ = -74.52\,kJ/mol$

However, in the implementation of biomass gasification to produce high quality syngas/or hydrogen, the formation of tars still offers a major technical challenge [6–9]. Tar formation creates numerous problems in gasifier operation, while conversion of tar adds value to the syngas by increasing the yields of H_2 and/or CO [10–12]. Therefore, the catalytic reforming of biomass tars into gaseous products is an effective and efficient method for tar removal, avoiding costly downstream processing for tar disposal [7,12,13].

An effective catalyst for biomass gasification should be stable and highly active, producing high quality and tar free synthesis gas. Dolomite, olivine, zeolites, alkali and noble metals, and Ni-based catalysts have been used for this purpose [5,6,12,13]. Ni catalyst is one of the most promising catalysts for biomass gasification due to its high reforming activity and affordability [14–18]. Deactivation may be an issue, however, with nickel-based catalysts [12,17–19]. Under the high operating gasification temperatures required to achieve significant feedstock conversions, Ni-based catalysts can be affected by deactivation. This can be attributed to coke deposition and crystallite agglomeration.

Thus, new catalysts for biomass steam gasification should have the long life required in preventing tar formation, carbon fouling and crystallite agglomeration under the operating conditions of a gasifier [5]. To accomplish this, the use of promoters plays a very important role in minimizing tar formation and in enhancing the stability of Ni-based catalysts [17–20]. Fluidizable γ-Al_2O_3 is one of the most promising supports for a Ni-based catalyst due to its high surface area and mechanical strength. The thermal stability of γ-Al_2O_3 can be enhanced through the addition of small amounts of La_2O_3 to the support phase [21–23]. Promoting effects of lanthanum on Ni/γ-Al_2O_3 catalysts have also been studied for steam reforming and dry reforming [16–18,24–30]. Addition of La_2O_3 improves the activity and stability of the catalyst by reducing metal-support interaction and increasing dispersion. Moreover, the basic La_2O_3 reduces the acidity of the support and enhances CO_2 adsorption resulting in lower coke formation on the catalyst surface. Furthermore, the catalyst preparation method also plays a crucial role influencing structural properties, metal-support interaction, reducibility and dispersion of active phase [31–33]. Conventionally, impregnated metal salts are decomposed to oxides by high temperature calcination in air followed by metal oxide reduction under hydrogen. Surface area, nickel dispersion and reducibility can be improved significantly, however, by direct decomposition of nickel salts to nickel in a reducing atmosphere without prior calcinations in air [31].

CREC researchers have contributed significantly to the development of active and stable Ni-based catalysts for steam and dry reforming [34–38]. CREC fluidizable catalysts may be of special relevance for a continuous industrial scale fluidized gasifier operation at 700 °C or close to 700 °C. This system could be implemented using twin circulating fluidized bed reactors. As a result, catalytic gasification could take place in one of these fluidized beds while catalyst regeneration could be done in the other unit. Under these conditions, both tar formation and ash agglomeration could be considerably reduced.

Most recently, a catalyst for steam gasification of biomass was developed using Ni on a fluidizable α-alumina support [39,40]. This study focuses, however, on the development, characterization and the evaluation of a new and improved fluidizable Ni catalyst supported on La_2O_3 modified γ-Al_2O_3. It is shown that the newly developed catalyst displays an encouraging performance in terms of conversion, yield and synthesis gas quality. In addition, experimental results have shown that this catalyst performance also ranks favorably with respect to gasification reaction equilibrium conditions.

2. Experimental methods

2.1. Catalyst preparation

In this study, Ni-based catalysts for biomass gasification were prepared via an 'incipient wetness' technique under vacuum conditions. In this respect, the following sequence of steps for catalyst preparation was established: (a) 100 μm γ-Al_2O_3 particles (Alcan Inc.) with 233 m^2/g surface area were used as the support, (b) γ-Al_2O_3 was modified by adding La_2O_3 (precursor: $La(NO_3)_3 \cdot 6H_2O$) and (c) following this, Ni (precursor: $Ni(NO_3)_2 \cdot 6H_2O$) was added on the modified γ-Al_2O_3 support. After the impregnation of metal nitrate solution, the resulting paste was dried slowly at 140 °C overnight. The dried powder was then reduced in a specially designed fluidized bed reactor at 700 °C (3 °C/min heating rate) for 8 h under a 10% H_2/He flow. Ni was loaded employing multi-step impregnation. Impregnation, drying and reduction steps were repeated until the desired loading was attained. In the case of 20 wt% Ni/5 wt% La_2O_3-γAl_2O_3 (Cat A), 8 consecutive steps were employed in nickel precursor impregnation. In order to establish the value of the La_2O_3 promoted Ni/γ-Al_2O_3 catalyst prepared via direct reduction of metal nitrate (Cat A), two other catalysts were prepared: (i) an unpromoted 20 wt% Ni/γAl_2O_3 (Cat C) and (ii) a 20 wt% Ni/5 wt% La_2O_3-γAl_2O_3 prepared via metal precursor calcinations in air at 700 °C (Cat B).

2.2. Catalyst characterization

2.2.1. BET analysis

The specific surface area, the average pore radius and pore volume of the prepared catalysts were determined in a Micromeritics ASAP 2010 Analyzer by N_2 adsorption at 77 K. For each experiment, 0.1–0.2 g of catalyst sample was degassed at 573 K for 2.5 h before the analysis. The adsorption isotherms were measured in 10^{-6}–1 relative pressure ranges.

2.2.2. Temperature programed studies

Temperature programed reduction (TPR), temperature programed oxidation (TPO), temperature programed desorption (TPD) and pulse chemisorption experiments were conducted using a Micromeritics Autochem II 2920 Analyzer. Before the hydrogen TPR experiment, the sample was pre-oxidized using a gas containing 5% oxygen in helium at 700 °C. The oxidized sample was then reduced at a heating rate of 10 °C/min using a gas containing 10% hydrogen in argon. The amount of hydrogen consumed (V_{H_2}) in the reduction of the catalyst sample was determined from the TCD signal. On the other hand, H_2 pulse chemisorption was performed at ambient temperature following the TPR experiment.

The quantity and strength of the acid sites on the support phase (γ-Al_2O_3) was determined using ammonia TPD. Before the TPD experiment, the catalyst sample was pre-treated by flowing He or H_2 (in case of Ni loaded samples) at 700 °C. The catalyst sample was then brought to saturation by flowing a stream of gas containing 5% NH_3 in Helium at 50 °C for 1 h. After 1 h purging, TPD was performed at a heating rate of 15 °C/min. To determine the basicity and CO_2 adsorption capacity of the catalyst samples, CO_2-TPD was performed using a similar procedure as used for NH_3-TPD.
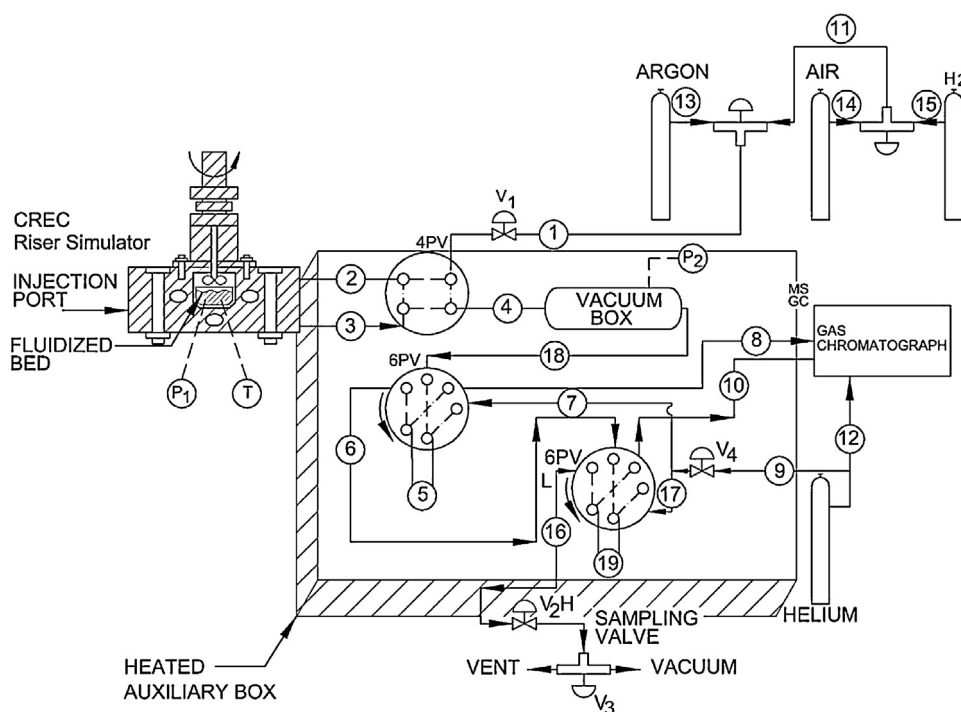
Fig. 1. Schematic diagram of the CREC Riser Simulator and its accessories. The 4PV allows: (i) isolation of the reactor for gasification to take place (when lines 2–3 are connected) and (ii) reactor evacuation (when lines 3–4 are connected). The two 6PVs permit: (i) loading sampling loops 5 and 19 with the lines 18–5–6 and 6–19–16 being connected, and (iii) directing the sample to the capillary and packed-bed column of the GC system through connection 7–5–8 and 17–19–10, respectively.

2.2.3. Pyridine FTIR

Pyridine FTIR was performed using a Bruker IFS55 FTIR Spectrometer. Before pyridine adsorption, the samples were heat treated at 500 °C under N_2 flow for 2 h and then cooled to 100 °C. Following this, the samples were saturated using a N_2 gas steam containing pyridine for 1 h. In the next step, the catalyst samples were purged with pure N_2 at 100 °C for 1 h, to remove weakly adsorbed pyridine. Finally, diffuse reflectance infrared spectroscopy (DRIFTS) measurements were recorded at room temperature using the Bruker IFS55 FTIR Spectrometer having a 4 cm^{-1} resolution and data averaging over 100 scans.

2.2.4. X-ray diffraction analysis

X-ray powder diffraction patterns were obtained on a Rigaku Miniflex diffractometer using Ni filtered Cu $K\alpha$ ($\lambda = 0.15406$ nm) radiation. A tube voltage of 40 kV and a tube current of 20 mA were used for each sample. The samples were scanned every 0.02° from 10° to 100° with a scan time constant of 2° min^{-1}. Identification of the phases were made with the help of the Joint Committee on Powder Diffraction Standards (JCPDS) files. The crystallite sizes of Ni were calculated using Scherrer's equation:

$$d = \frac{0.94\lambda}{(\beta - \beta_o)\cos\theta}$$

where, d is the volume average diameter of the crystallite and $(\beta - \beta_o)$ is the full width at half maximum of the peak.

2.3. Biomass gasification in the CREC Riser Simulator

Steam gasification of glucose (a model compound of biomass) was performed using a CREC Riser Simulator by varying temperature, steam/biomass (S/B) ratio and reaction time. The CREC Riser Simulator is a bench-scale mini fluidized bed reactor with a volume of 50 cm^3. This bench-scale reactor is specially designed for catalyst evaluation under the operating conditions of an industrial

fluidized bed reactor. A schematic diagram of the CREC Riser Simulator experimental setup is shown in Fig. 1. A detailed description of the CREC Riser Simulator can be found elsewhere in the literature [41].

The Ni catalysts, already thermally treated during the preparation stage, were loaded into the catalyst basket. The reactor system was sealed, leak tested and heated to the reaction temperature in an argon atmosphere. Then, the glucose water solution was injected, and once the reaction time was reached, the reaction products were evacuated from the reactor to the vacuum box. Reactor and vacuum box pressure data against time were recorded by the Personal Daq Acquisition Card.

Fig. 2 displays the pressure changes in the reactor unit (upper curves) and vacuum box (lower curves), during glucose gasification. One can notice that as soon as the water glucose solution was
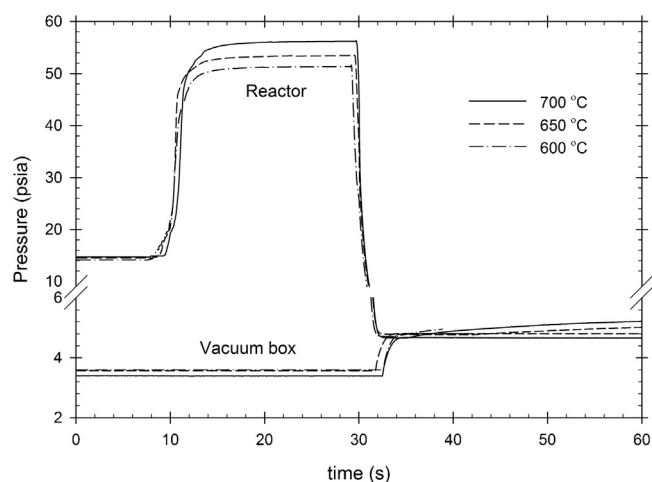

Fig. 2. Pressure changes in the reactor and vacuum box of the CREC Riser Simulator during glucose gasification using Cat A at different temperatures, S/B = 1.0 g/g and 20 s of reaction time.
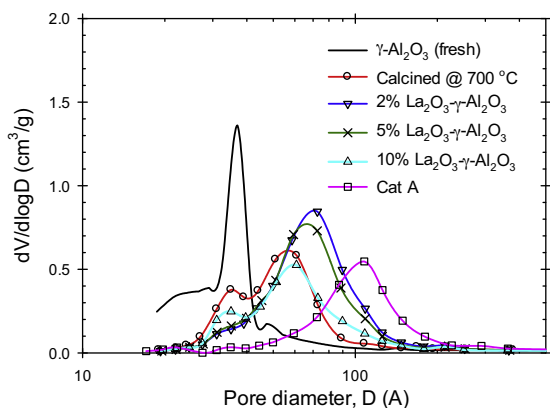
Fig. 3. Pore size distribution of support and catalyst samples.

injected, the pressure in the reactor increased sharply (first second) and then more gradually (remaining 20 s). These total pressure changes are likely due to the quick glucose solution vaporization and conversion (primary gasification reactions), followed by much slower inter-conversion of gas phase species (secondary gasification reactions). Fig. 2 also shows that as the temperature increased, higher reactor pressure readings were observed indicating higher gas yields.

From the vacuum box, gas samples were sent to a GCMS system via heated transfer lines. The GCMS system is equipped with a packed-bed column (HaysSep® D) and a capillary column (BPX5). The packed-bed column is connected to a thermal conductivity detector (TCD) and the capillary column is connected to a mass spectrometer (MS).

To burn the coke deposited on the catalyst, a regeneration cycle was performed. The regeneration conditions were 10 min of air flow and 10 min of hydrogen flow (to reduce the catalyst). Under these conditions, coke was completely removed. Finally, the coke deposited on the catalyst after the experimental runs was measured as CO_2 in a Total Organic Carbon Analyzer (TOC-V) using a solid sample module (SSM-5000). All experiments were repeated at least 4 times to secure reproducibility of the results. Standard deviations for experimental repeats were in the 3–10% range with an average of 5%. An important observation from these runs was that the mass balance closures, which included H_2, CO, CO_2, H_2O, CH_4, ethylene, ethane, propylene, acetaldehyde, and carbon deposited over the catalyst, were in the ±15% range, with most of the mass balances closing in the ±5% range.

3. Experimental results

3.1. Catalyst characterization

3.1.1. BET surface area analysis

Table 1 reports BET surface area, pore volume and average pore diameter for both the support materials and Ni catalysts determined using N_2 adsorption–desorption. The pore size distribution, as described in Fig. 3, were determined by analyzing the desorption branch of the isotherm and using the BJH (Barrett–Joyner–Halenda) method.

As shown in Table 1, the BET surface area of the fresh γ-Al_2O_3 was found to be 233 m²/g. However, both the surface area and the pore volume of the γ-Al_2O_3 were reduced drastically after calcination at 700 °C for 6 h, while the pore diameter increased from 38 to 72Å due to calcination. According to the technical literature [21–23,27,42,43], this decrease in surface area with an increase in pore diameter can be attributed to the thermal sintering of γ-Al_2O_3 due to the surface diffusion of γ-Al_2O_3. Schaper et al. [22] consider

that thermal treatment redistributes the material in the solid state in order to decrease surface energy causing losses of surface area.

However, with the incorporation of La_2O_3 in an amount as low as 2 wt%, S_{BET} increased from 116 to 124 m²/g while compared to bare calcined γ-Al_2O_3. This increase in surface area for lanthanum modified γ-Al_2O_3 is in agreement with the data reported in the literature [21,22,27,42]. Lanthanum is considered to augment the γ-Al_2O_3 thermal resistance by reducing the number of sites where α-Al_2O_3 nucleation can occur [42]. On the other hand, with the addition of 2 wt% La_2O_3, the average pore diameter is increased up to 84 Å which suggests the blocking of some small pores by La_2O_3.

The thermal stability of γ-Al_2O_3 was further increased by raising the La_2O_3 content up to 5 wt%. This was consistent with an increase in surface area and a reduction in pore diameter (Table 1). However, a further increase of La_2O_3 content up to 10 wt%, diminished both surface area and pore volume. This was ascribed to pore blocking and/or to the introduction of La_2O_3 particles into the gamma-alumina pore network. Moreover, the data obtained was considered an indication that the addition of lanthanum oxide beyond approximately 5 wt%, does not help to further improve the thermal stability of the support phase.

With the nickel incorporation to the lanthanum modified support (Cat A-1, Cat A-2 and Cat A in Table 1), both specific surface area and pore volume were diminished. There was also a gradual increase in pore diameter. In fact, after impregnating 20 wt% Ni (Cat A), the surface area was reduced to 55.5 m²/g and the average pore diameter increased to 124 Å. These catalyst structural changes can be attributed to the relative high loading of Ni and the inclusion of large-size metal particles into the support pores. Furthermore as reported in Table 1, Ni directly supported on undoped γ-Al_2O_3 (Cat C) led to a catalyst with a much smaller specific surface area (31.3 m²/g) and larger average pores (151 Å).

3.1.2. Acid–Base properties

The support acidity and basicity have a significant effect on the catalytic activity and the resistance to coke deposition. The type and nature of acidic sites present in γ-Al_2O_3 and in the La_2O_3 modified γ-Al_2O_3 support were evaluated with DRIFT using pyridine as a probe molecule. Pyridine interacts with different acid sites through the electron lone pair of its nitrogen atoms. Three types of adsorbed pyridine species have been reported as being present [44–46]: (a) molecularly adsorbed pyridine coordinating its lone electron pair from the nitrogen atom at surface Lewis acid sites (Al^{3+}), (b) hydrogen-bonded pyridine via its nitrogen atom to weakly acidic hydroxy surface sites, and (c) pyridinium ion formed by extracting a proton from a Brønsted acid hydroxy surface site. In this respect, the "8a-8b" and "19a-19b" stretching vibrational modes of the pyridine ring are the most sensitive modes that can be evaluated to assess adsorption interaction strength using IR. More specifically, protonated pyridine on Brønsted centers give bands at 1640 and 1540 cm⁻¹. Furthermore, bands in the 1590–1635 cm⁻¹ and 1440–1455 cm⁻¹ ranges are characteristic of pyridine coordinated with Lewis acid sites [44–47]. One should notice that the "19a" vibration band at around 1490 cm⁻¹ is less informative, as it is associated with all three types of adsorbed pyridine.

Fig. 4 reports the IR spectra of the undoped γ-alumina support, following pyridine adsorption and evacuation at 100 °C for the 1700–1400 cm⁻¹ spectral region. One can notice that the bare γ-alumina sample did not show a 1540 cm⁻¹ band. This demonstrates that there are no Brønsted acid sites on the γ-alumina surface strong enough to form pyridinium ions. The appearance, however, of the "19b band' at 1445 cm⁻¹ and the "8a bands" at 1595 and 1615 cm⁻¹ in the DRIFT spectra of undoped alumina, reveals the presence of Lewis acid sites.

Furthermore, the technical literature reported an "8a band" for pyridine, providing information about three possible types

Table 1
BET surface area, pore volume and pore diameter of the support and catalyst samples.

Sample	S_{BET} (m^2/g)	Pore volume (cm^3/g)	Avg pore dia (Å)
γ-Al$_2$O$_3$	233	0.25	38
γ-Al$_2$O$_3$ calcined @ 700 °C	116	0.23	72
2% La$_2$O$_3$-γ Al$_2$O$_3$	124	0.28	84
5% La$_2$O$_3$-γ Al$_2$O$_3$	130	0.26	75
10% La$_2$O$_3$-γ Al$_2$O$_3$	115	0.23	74
10% Ni/5% La$_2$O$_3$-γ Al$_2$O$_3$ (Cat A-1)	77.5	0.21	108
15% Ni/5% La$_2$O$_3$-γ Al$_2$O$_3$ (Cat A-2)	66.2	0.20	114
20%Ni/5% La$_2$O$_3$-γ Al$_2$O$_3$ (Cat A)	55.5	0.19	124
20%Ni/5% La$_2$O$_3$-γ Al$_2$O$_3$ (Cat B)	70.5	0.19	115
20%Ni/γ Al$_2$O$_3$ (Cat C)	31.3	0.16	151

of Lewis acid sites with different strengths [48–50]: (i) weak (1590–1610 cm^{-1}), (ii) moderate (1610–1620 cm^{-1}) and (iii) strong (1620–1635 cm^{-1}). As a result, the observed peaks in Fig. 4 at 1595 cm^{-1} and 1615 cm^{-1} for undoped γ-Al$_2$O$_3$ indicate the presence of weak to moderate Lewis acid sites. Regarding the small peak at 1576 cm^{-1} corresponding to the "8b" vibrational mode is either hydrogen bonded or coordinated pyridine. Thus, this peak does not provide specific acid site information.

One can also notice that in the case of γ-Al$_2$O$_3$ modified with 5 wt% La$_2$O$_3$, the intensities of all the '19a,b' and "8a,b" bands were significantly reduced. Furthermore, when La$_2$O$_3$ loading was increased from 5% to 10%, essentially all the peaks disappeared except for a small peak at 1447 cm^{-1}. These results show the effect of La$_2$O$_3$ in decreasing the acidity of γ-Al$_2$O$_3$.

The acidity and basicity of the supports were further investigated by temperature programed desorption (TPD) of different probe molecules. Fig. 5 reports NH$_3$-TPD profiles for the undoped and La$_2$O$_3$ doped γ-Al$_2$O$_3$ supports, and the Ni catalyst. One can notice that the undoped γ-Al$_2$O$_3$ yields an asymmetric desorption peak in the low temperature range of 50 to 450 °C. This peak displays a maximum at around 120 °C and a long tail. The low temperature desorption peaks confirm the absence of Brønsted acid sites while the tail can be attributed to the presence of Lewis acid sites with different strengths. Total acidities of the catalyst samples were calculated from the NH$_3$ desorption and listed in Table 2.

Regarding total acidity, one can notice in Table 2 that with the addition of the 2 wt% La$_2$O$_3$, the total acidity of γ-Al$_2$O$_3$ was decreased from 370 to 272 µmol NH3/g γ-Al$_2$O$_3$. As well, a 5 wt% La$_2$O$_3$ addition yielded a further decrease in the acidity of the γ-Al$_2$O$_3$ surface. Augmenting La$_2$O$_3$ content to 10 wt%, did not

result in substantial reduction in total acidity, exhibiting however, a higher concentration of acid sites. This confirms that the addition of La$_2$O$_3$ up to 5 wt% helps to diminish the abundance of acid sites on the γ-Al$_2$O$_3$ surface.

In the case of a 20 wt% Ni/5 wt% La$_2$O$_3$-γ Al$_2$O$_3$ catalyst (Cat A), the total acidity is substantially decreased to 97 µmol NH$_3$/g γ-Al$_2$O$_3$. One should mention that this significant reduction of acidity may be a combined effect of Ni addition and changes in the γ-Al$_2$O$_3$ support during Ni impregnation. For instance, 20% Ni was loaded using 8 successive impregnations with overnight reduction at 700 °C following every impregnation step. When 20 wt% Ni was added, however, on the 5 wt% La$_2$O$_3$-γAl$_2$O$_3$, the catalyst specific surface area diminished from 130 to 55.55 m^2/g. If one considers a total acidity defined on a per unit surface area, the total acidity was then reduced from 1.85 to 1.41 µmol NH$_3$/m^2 (Table 2) only for the 20 wt% Ni loading.

Concerning Cat C, a higher acidity (137 µmol NH$_3$/g γ-Al$_2$O$_3$) with respect to Cat A was found. Moreover, the catalyst prepared with precursor calcination instead of direct reduction (Cat B), exhibited significantly higher acidity (162 µmol NH3/g γ-Al$_2$O$_3$) than either Cat A or Cat C. Acidity data from Cat B can be justified given the low exothermicity of the metal precursor decomposition under air yielding modest losses in surface acidity. On the other hand, Cat A and Cat C acidity data can be explained given the higher heat evolved when the Ni precursor is transformed under hydrogen giving larger losses in surface acidity [31].

CO$_2$-TPD profiles of La$_2$O$_3$ doped and bare γ-Al$_2$O$_3$ are reported in Fig. 6. Results are summarized in Table 2. The calcined γ-Al$_2$O$_3$ support gave a single asymmetric low-temperature (45 to 275 °C) peak of CO$_2$ desorption with a maximum value at 95 °C. According to Morterra et al. [51], this low-temperature desorption peak can be attributed to the low-strength basic sites. These low-strength
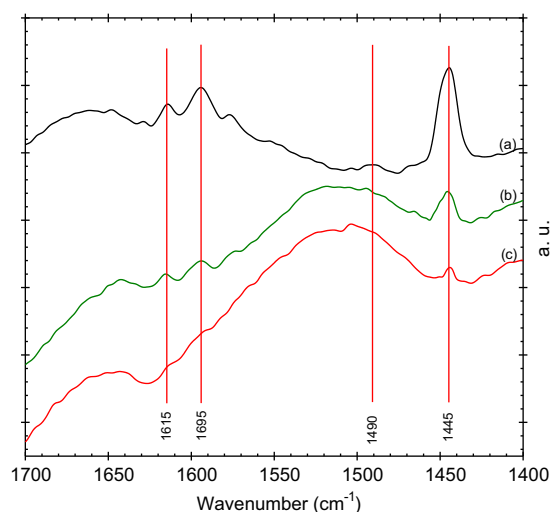

Fig. 4. DRIFT spectra of La$_2$O$_3$ modified γ-Al$_2$O$_3$ samples: (a) bare γ-Al$_2$O$_3$, (b) 5% La$_2$O$_3$-γ-Al$_2$O$_3$ and (c) 10% La$_2$O$_3$-γ-Al$_2$O$_3$.
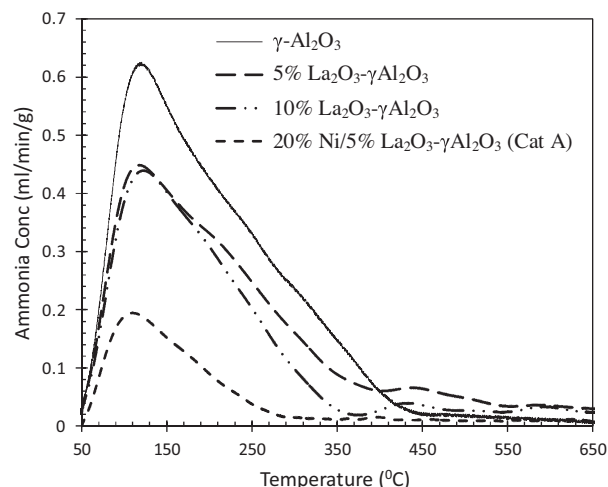

Fig. 5. NH$_3$-TPD profile of support and catalyst samples.

Table 2
Total acidity and basicity of the support and catalyst samples as determined from NH_3-TPD and CO_2-TPD, respectively.

Sample	Total acidity		Total basicity	
	μmol/g γ-Al_2O_3	μmol/m^2	μmol/g γ-Al_2O_3	μmol/m^2
γ-Al_2O_3 calcined	370	3.18	91	0.79
2% La_2O_3-γ Al_2O_3	272	2.15	105	0.83
5% La_2O_3-γ Al_2O_3	251	1.85	131	0.96
10% La_2O_3-γ Al_2O_3	250	1.96	156	1.22
Cat A-1	135	1.41	121	1.47
Cat A-2	111	1.40	96	1.21
Cat A	97	1.39	83	1.19
Cat B	162	1.85	69	0.79
Cat C	137	3.63	38	1.01

basicity sites could be traced to bicarbonates, which are formed as a result of the interaction between CO_2 and the weak basic surface hydroxyl groups. In addition, the asymmetric CO_2 desorption peak shows the coexistence of basic sites of different strengths. As reported in Fig. 6, La_2O_3 addition significantly increases basic density and site strength. Furthermore, the CO_2 adsorption capacity increased from 105 to 156 μmol CO_2/g γ-Al_2O_3 when the La_2O_3 content increased from 2 to 10 wt%. Regarding the influence of basicity, it has been reported that catalysts having a higher basicity support show stronger resistance to carbon fouling during steam and dry hydrocarbon reforming [52–56]. It is thus hypothesized that a basic support could improve the adsorption capacity of acidic CO_2, so that more coke could be eliminated from the catalyst surface according to the Boudouard reaction ($C + CO_2 \leftrightarrow 2CO$).

Regarding the Ni catalysts, total basicity was gradually decreased at higher Ni contents (Table 2). When Ni was increased from 10 to 20 wt%, the CO_2 adsorption was reduced from 131 to 83 μmol CO_2/g γ-Al_2O_3. This was due to the partial blockage of basic sites by the impregnated nickel. Moreover, for the catalyst prepared by calcination (Cat B), the basicity after Ni impregnation was further decreased to 69 μmol CO_2/g γ-Al_2O_3. Furthermore, for the unpromoted Ni/γ-Al_2O_3 catalyst (Cat C) significantly lower CO_2 desorption (38 μmol CO_2/g γ-Al_2O_3) was obtained.

3.1.3. Reducibility, dispersion and crystal size

Reducibility (R), dispersion (D) and crystal size (d_v) of the active phase are summarized in Table 3. The focus of this study is to conduct steam gasification of biomass at a temperature below 700 °C to avoid ash agglomeration and other operational issues with gasifiers. Therefore, reducibility below 700 °C ($R_{700 °C}$) is an important characteristic to investigate and is given in Table 3 as well. Fig. 7 shows the TPR profiles of La_2O_3 doped and undoped Ni catalysts as

well as the profile for the La_2O_3 modified γ-Al_2O_3 support. The TPR profile of the La_2O_3-γAl_2O_3 support does not show any peak with the hydrogen consumed being negligible.

Fig. 7 shows that the Ni catalyst supported on bare γ-Al_2O_3 (Cat C) gives wide reduction peaks in the 350 °C to 950 °C range, with four peaks at 400, 460, 640 and 800 °C. The first peak (at 400 °C) can be assigned to the reduction of highly dispersed NiO species on the support surface [27,42,43]. According to the literature [24,42,43,57], the second peak (460 °C) can be attributed to the reduction of NiO particles which are deposited on the support, yielding pores with limited chemical species accessibility. Deposition of active metals into the pores is also predicted by BET results. The third peak at 640 °C can be assigned to the reduction of highly dispersed non-stoichiometric amorphous nickel-aluminate spinels [24,27,57]. Finally, the reduction peak observed above 700 °C is related to the reduction of bulk nickel-aluminate ($NiAl_2O_4$) [24,27,42,43,57,58].

When using lanthanum modified Ni/γ-Al_2O_3 catalysts (Cat A), reduction peaks were shifted to lower temperatures (Fig. 7). Compared to the Ni catalyst on bare alumina, La_2O_3 addition yields a higher proportion of easily reducible NiO species as well as reduced $NiAl_2O_4$ formation significantly. Sanchez-Sanchez et al. [24,57] and Hossain et al. [23], also reported the increase in reduction intensities of NiO using La_2O_3 doped Ni catalysts. Therefore, the addition of lanthanum on the alumina support, as reported in Table 3, significantly improved the catalyst reducibility below 700 °C from 66 to 87%. Furthermore, lanthanum addition facilitated the dispersion of Ni (0.9 to 1.12%) resulting in Ni crystallites of reduced size (108 to 87 nm).
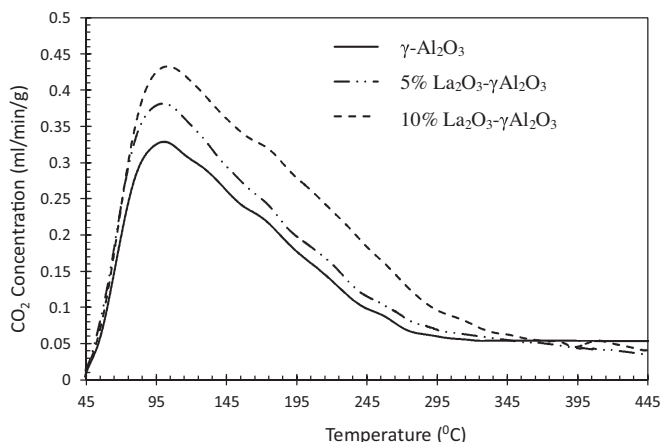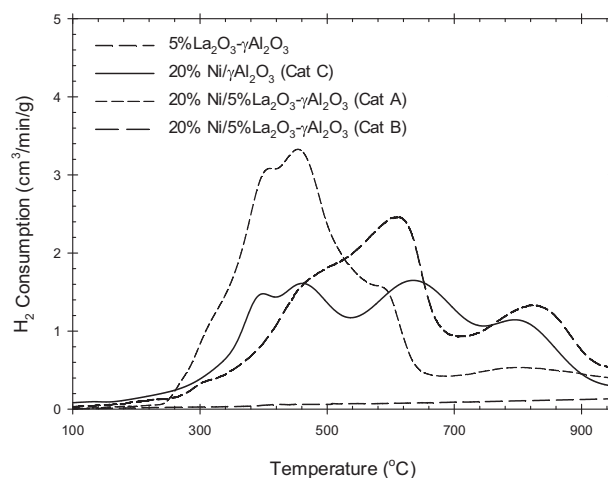

Fig. 6. CO_2-TPD profile of La_2O_3 modified γ-Al_2O_3 support.

Fig. 7. TPR profiles of the La_2O_3 modified γ-Al_2O_3 and supported Ni catalysts (using 10% H_2 with balanced Ar at a flow rate of 50 cm^3/min and at a 10 °C/min heating rate).

Table 3
Reducibility (R), dispersion (D) and crystal size (d_v) of Ni for different catalysts.

Sample	R (%)	$R_{700\,°C}$ (%)	$D(\%) = 117X/WR$	$d_v(\text{nm}) = 97.1/\%D$
10%Ni/5% La$_2$O$_3$–γ Al$_2$O$_3$ (Cat A-1)	94	71	1.67	58
15%Ni/5% La$_2$O$_3$–γ Al$_2$O$_3$ (Cat A-2)	92	83	1.32	73
20%Ni/5% La$_2$O$_3$–γ Al$_2$O$_3$ (Cat A)	91	87	1.12	87
20%Ni/5% La$_2$O$_3$–γ Al$_2$O$_3$ (Cat B)	83	66	0.92	106
20%Ni/γ Al$_2$O$_3$ (Cat C)	81	66	0.90	108

X stands for the total hydrogen chemisorbed (μmol of H$_2$/g cat); W denotes the metal loading (wt%).

Fig. 7 also reports TPR profile of the catalyst prepared with precursor decomposition via calcination (Cat B). It can be observed that Cat B yields significantly lower amounts of reducible species (only 83%) while compared to Cat A. Moreover, Cat A display a significantly larger proportion of easily reducible surface NiO sites than Cat B, with Cat B having higher levels of undesirable NiAl$_2$O$_4$. According to Bartholomew and Farrauto [31], the calcination of Ni nitrates favors the formation of large NiO particles as well as the formation of very stable NiAl$_2$O$_4$ through the interaction of NiO and Al$_2$O$_3$. Therefore, Cat B exhibited very low $R_{700\,°C}$ (66%) and dispersion of nickel. On the basis of these findings, one can argue that direct decomposition of the metal nitrates to a metallic species in hydrogen is critical especially when the metal loading onto the support is accomplished in several steps.

Regarding metal loading, one can notice that augmenting active metal (Ni) content leads to a reactivity increase. Fig. 8 reports TPR profiles of Ni/γAl$_2$O$_3$ catalysts modified with 5 wt% lanthanum oxide containing 10, 15 and 20 wt% Ni. It is thus apparent from Fig. 8 that increasing Ni content, leads to a significant increase in the easily reducible NiO species. In fact, when Ni loading is raised from 10 to 20%, $R_{700\,°C}$ augments from 71% to 87%. This finding also confirms the advantage of muti-step impregnation used in the 20 wt% Ni catalyst preparation, yielding a higher density of reducible active sites.

3.1.4. Stability test

In biomass gasification, the catalyst undergoes repeated oxidation-reduction cycles in the gasifier and the catalyst regeneration units. Therefore, a critical characteristic of a catalyst for biomass gasification is its stability under cyclic operation. To investigate these matters, successive TPO and TPR experiments were developed. Each cycle was composed of successive TPO, TPR, and pulse chemisorption experiments. Fig. 9 reports reducibility, dispersion and size of the Ni crystals of Cat A under repeated oxidation and reduction cycles.

One should mention that almost identical TPR profiles were found even after ten cycles of TPO/TPR experiments. It can be further observed in Fig. 9 that percentage reduction almost remained same under the repeated TPO/TPR cycles. The 20% Ni/5% La$_2$O$_3$-γAl$_2$O$_3$ (Cat A) showed stable reducibility over repeated oxidation-reduction cycles with an average reduction percentage of 91.1%. Pulse chemisorption results further confirm the stability and negligible metal crystallite agglomeration of the catalyst over repeated oxidation-reduction conditions with consistent percentage dispersion and crystal size of Ni. These results indicate that the catalyst preparation via multi-step impregnation with reduction of samples after each impregnation in fluidized bed conditions is an effective way to prepare stable catalysts to sustain the harsh operating conditions of an industrial gasifier unit.

3.2. Gasification results

Cellulose is a main carbohydrate constituent of biomass. Typically, cellulose content in biomass ranges from 22.5 to 50.3 wt%. Cellulose is a polymer of glucose with a repeating unit of C$_6$H$_{10}$O$_5$ strung together by ß-glycosidic linkages [5]. On this basis, glucose was chosen as a model compound for the cellulose contained in biomass, to evaluate the steam gasification performance of the Ni catalyst supported by La$_2$O$_3$ modified γAl$_2$O$_3$. Performance of the catalysts were evaluated in terms of (a) carbon conversion to permanent gases, (b) dry gas yield (moles of H$_2$, CO, CO$_2$, H$_2$O, and CH$_4$ produced/moles of glucose fed), (c) coke deposition (% of C injected) and (d) product composition. To compares the performance of the prepared catalysts, gasification experiments were performed at 650 °C using a steam/biomass ratio of 1.0, a Cat/Biomass ratio of 12.5 and 20 s reaction time.
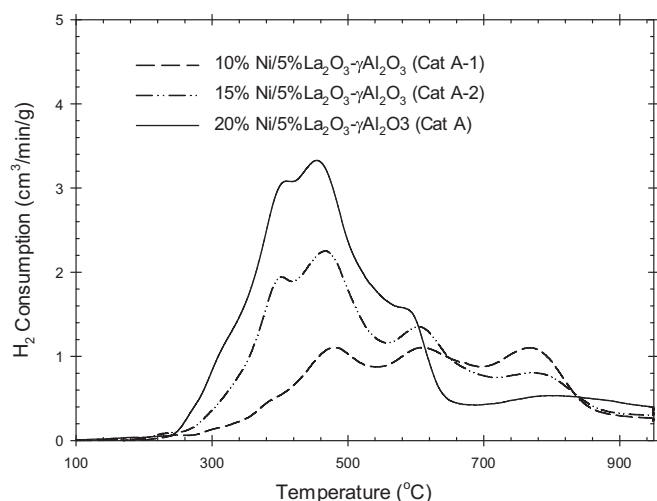

Fig. 8. TPR profiles of catalysts with different Ni content (using 10% H$_2$ with balanced Ar at a flow rate of 50 cm^3/min and 10 °C/min heating rate).
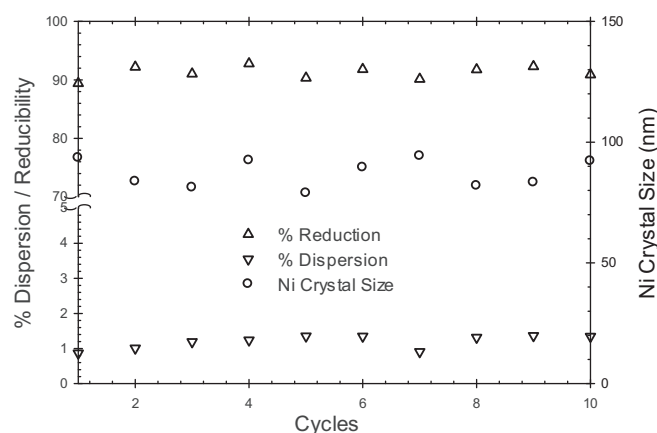

Fig. 9. Reducibility, dispersion and crystal size of a 20% Ni/5% La$_2$O$_3$–γAl$_2$O$_3$ (Cat A) catalyst over TPO/TPR cycles. (oxidizing agent: 5% O$_2$ in He; reducing agent: 10% H$_2$ in Ar; flow rate: 50 cm^3/min; heating rate: 10 °C/min).

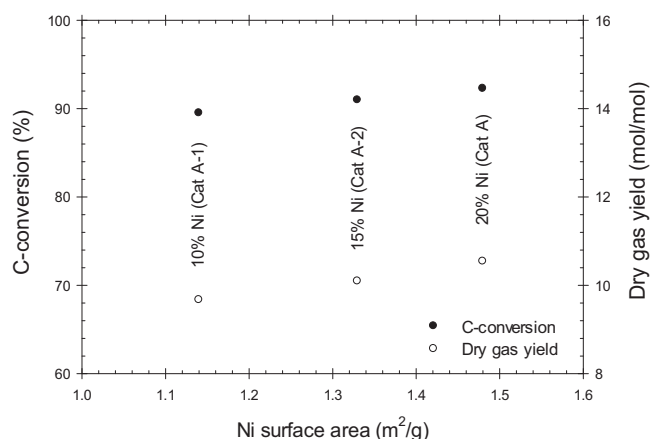**Fig. 10.** C-conversion and dry gas yield as a function of Ni surface area. [650 °C, $S/B = 1.0$ g/g; catalyst/biomass = 12.5; 20 s reaction time].

3.2.1. Effect of Ni loading

The available surface area of the active phase (Ni) is a crucial determinant of catalyst reactivity. Ni surface area, which can be calculated from Ni loading and dispersion, was varied significantly in the present study, when the Ni loading was increased from 10 wt% (Cat A-1) to 20 wt% (Cat A). The total acidity and basicity also varied with Ni loading, as shown in Table 2. However, their ratio remained almost unchanged among Cat A-1, Cat A-2 and Cat A.

Fig. 10 reports the carbon conversion and dry gas yield from glucose gasification using a Ni/5 wt% La_2O_3-γAl_2O_3 with varying Ni content. Fig. 10 shows that with the increase of Ni loading, the available Ni surface area is augmented gradually resulting in both higher dry gas yield and carbon conversion. Fig. 11 reports the composition of the main products from gasification. It shows that the increase of Ni loading from 10 wt% (Cat A-1) to 20 wt% (Cat A), yields higher H_2 with a significantly reduced CH_4 (16 to 12 mol%) content. This indicates that a higher Ni surface area facilitates the methane reforming reactions. Furthermore, the increase in CO_2 and the decrease in CO also confirms that the available Ni enhances the water gas-shift activity. Furthermore, higher Ni yields lower coke, which is an indicator of the greater extent of coke reforming: 6.5% versus 4.4% for an increase in Ni loading from 10 to 20 wt%.

3.2.2. Effect of preparation method and La_2O_3 addition

In order to establish the influence of lanthanum addition and the effect of the catalyst preparation method, gasification performance
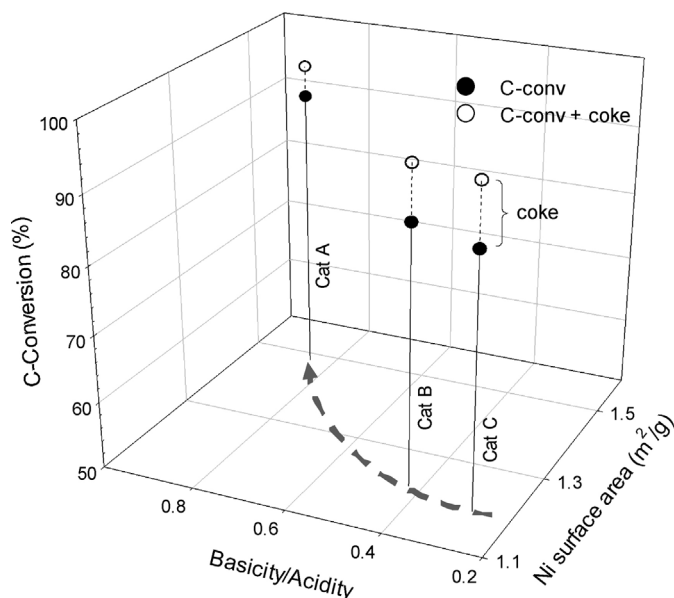

Fig. 12. C-conversion as a function of Ni surface area and Basicity/Acidity ratio. [650 °C, $S/B = 1.0$ g/g; catalyst/biomass = 12.5; 20 s reaction time].

of the following catalysts were compared: (a) 5 wt% La_2O_3 promoted 20% Ni/γAl_2O_3 (Cat A) with metal precursor being reduced, (b) 20 wt% Ni/5 wt% La_2O_3-γAl_2O_3 with metal precursor being calcined (Cat B) and (c) unpromoted 20 wt% Ni/γAl_2O_3 (Cat C). Besides Ni dispersion, total acidity and total basicity, and basicity/acidity ratio of the catalysts were also significantly varied among Cat A, Cat B and Cat C as reported in Table 2. The acid sites of a catalyst are responsible for hydrocarbon cracking, whereas the basic sites promote coke/char reforming facilitating H_2O and CO_2 adsorption [17,18,59].

Fig. 12 reports the carbon conversion to permanent gases and the degree of coke deposition as functions of the both Ni surface area and basicity/acidity ratio. Fig. 12 also describes how the Ni surface area and the basicity/acidity ratio change when moving from Cat C to Cat B to Cat A. Consistent with this, carbon conversion to permanent gases is also augmented from 87.5% to 88.6% and 92.3% when using Cat C, Cat B and Cat A, respectively. Fig. 12 also reports that a concurrent reduction in coke deposition with the observed improvement of C-conversion: coke is diminished from 8.9 to 4.4% when using Cat A instead of Cat C.
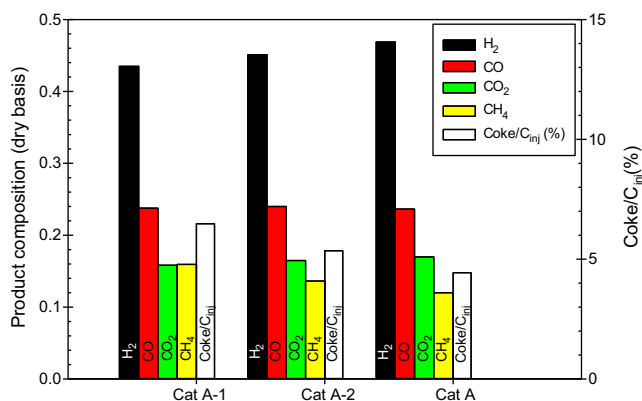

Fig. 11. Product composition and coke deposition from glucose gasification using Ni/5 wt% La_2O_3-γAl_2O_3 catalysts containing 10 wt% Ni (Cat A-1), 15 wt% Ni (Cat A-2) and 20 wt% Ni (Cat A). [650 °C, $S/B = 1.0$ g/g; catalyst/biomass = 12.5; 20 s reaction time].
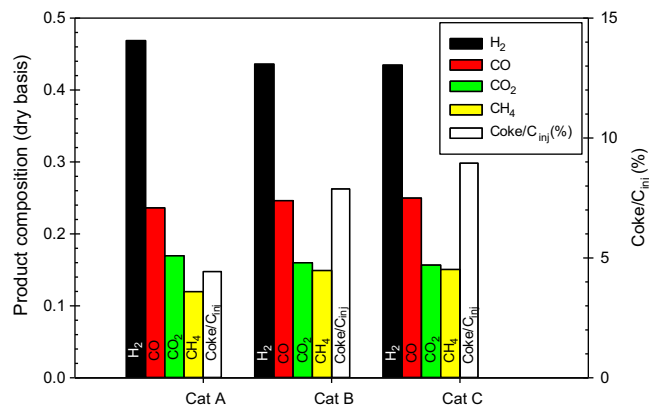

Fig. 13. Product composition and coke deposition from glucose gasification using a Ni/La_2O_3-γAl_2O_3 catalyst prepared via direct reduction of metal nitrate precursors (Cat A), Ni/La_2O_3-γAl_2O_3 prepared via metal precursor calcinations (Cat B) and unpromoted Ni/γAl_2O_3 (Cat C). [650 °C, $S/B = 1.0$ g/g; catalyst/biomass = 12.5; reaction time = 20 s.].
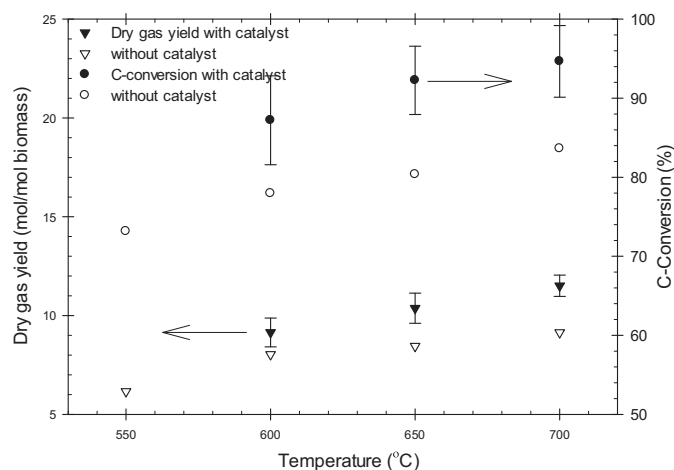
Fig. 14. Changes of (a) dry gas yield and (b) carbon conversion, with temperature during glucose gasification using a Cat A (20% Ni/5% La$_2$O$_3$-γAl$_2$O$_3$) and without a catalyst. [S/B = 1.0 g/g; catalyst/biomass = 12.5; 20 s reaction time].

Fig. 13 reports the composition of gasification products. It can be noticed that moving from Cat C to Cat A, yields higher amounts of H$_2$. These results suggests that in the case of Cat A, there is a greater extent of coke reforming with this being assigned to the higher Ni surface area and a higher basicity/acidity ratio. To estimate the extent of coke reforming reactions, yields of main product components were analyzed. It was found that only the heterogeneous water–gas shift reaction has a forward driving force, whereas the Boudouard and hydrogenating gasification reactions remain close to equilibrium or act in reverse. Thus, coke reforming likely occurs via heterogeneous water–gas shift reaction (C + H$_2$O + H$_2$ + CO) producing more H$_2$ and CO. Cat A also yields reduced methane (15 to 12 mol%), showing its higher methane reforming activity when compared to Cat B and Cat C. Fig. 13 also reports that CO$_2$ is slightly increased while CO is decreased when moving from Cat C to Cat B to Cat A. This result strongly suggests an increased water gas-shift activity for Cat A than Cat B and Cat C.

On this basis, it can be concluded that the 20%Ni/5%La$_2$O$_3$-γAl$_2$O$_3$ catalyst prepared via direct reduction (Cat A), displays structural properties favorably affecting glucose gasification. This favorable Cat A performance was confirmed by using a wide range of temperatures, steam biomass ratios (S/B) and reaction time conditions. The experimentally obtained data were also compared with the product chemical species fractions at thermodynamic equilibrium. It is valuable to observe that the experimentally obtained chemical species fractions for Cat A as will be reported later, are close to equilibrium values calculated using the method proposed by Salaices et al. [39]. In the present research, however, this thermodynamic equilibrium model also includes the system total pressure.

3.2.3. Effect of temperature

Fig. 14 reports the changes in dry gas yield and in the carbon conversion of glucose gasification using 20% Ni/5% La$_2$O$_3$-γAl$_2$O$_3$ (Cat A) and without catalyst at various temperatures. Both the dry gas yield and the carbon conversion are increased with temperature in both catalytic and non-catalytic experiments. It is considered that the higher temperatures favor steam and dry reforming of hydrocarbons, heterogeneous water–gas shift and Boudouard reactions. As shown in Fig. 14, if the temperature is raised from 600 to 700 °C, the dry gas yield augments from 9.15 to 11.5 mol/mol of glucose and the carbon conversion is increased from 87 to 95%.

It can also be noticed in Fig. 14 that both the dry gas yield and the carbon conversion improved substantially in all catalytic experiments while compared to the non-catalytic runs. In fact, the use

of Cat A increased the dry gas yield on average by 20%. However, the effect of the catalyst is more prominent at higher temperatures. This means that the catalyst activity for various gasification reactions increases with temperature, with this being especially true for steam and dry reforming of hydrocarbons. Moreover, the dry gas yield achieved for the catalytic gasification of glucose at 600 °C is higher than the one for non-catalytic experiments at 700 °C. Similarly, using the catalyst of the present study, carbon conversion is increased by approximately 12.5% on average.

Fig. 15 reports H$_2$, CO, CO$_2$ and CH$_4$ compositions (dry basis) in the product gas with temperature variation using the Ni catalyst of the present study. One can notice an increase in H$_2$ composition with the increase in temperature. This can be assigned to the higher influence of steam and dry reforming of hydrocarbons on the overall reaction network. Raising the temperature also has important effects on CO composition. Due to the increased influence of reforming, heterogeneous water–gas shift and Boudouard reactions, higher gasification temperatures also lead to higher CO (Fig. 15b). When temperature is increased from 600 to 700 °C, CO composition increases almost linearly from 20 to 28%.

Fig. 15c and d shows that at higher thermal levels both the CO$_2$ and CH$_4$ compositions are decreased. One can notice low methane concentrations in the product gas at higher temperatures (5.8% at 700 °C). These low methane levels are a primary indication of the high methane reforming activity of the catalyst used in this study.

Salaices et al. [39,40] also reported H$_2$, CO, CO$_2$ and CH$_4$ product compositions (dry basis) obtained from glucose gasification and their changes with the temperature. These data were obtained at the same operating conditions as the ones of present study. In the experiments by Salaices et al. [39,40], a 2.5% Ni/α-Al$_2$O$_3$ catalyst was used with a catalyst/biomass for 25 g/g. This catalyst/biomass ratio was double with respect to the 12.5 g/g of the present study. Comparing the results obtained by Salaices et al. [39,40] to the findings of the present study, one can notice that significantly higher H$_2$ and CO$_2$, and lower CO and CH$_4$ compositions were obtained in our study using half the amount of catalyst, as shown in Fig. 15. These data confirmed that the 20% Ni/5%La$_2$O$_3$-γAl$_2$O$_3$ catalyst displays higher steam reforming, dry reforming and water–gas shift activity than the 2.5% Ni/α-Al$_2$O$_3$. This higher catalytic activity can be attributed to the following: (i) higher Ni content (20 wt% instead of 2.5 wt%), (ii) higher specific surface area (55.55 instead of 22.4 m^2/g), (iii) higher reducibility (91% versus 76%), and (iv) addition of La$_2$O$_3$ which is known to catalyze coke reforming reactions.

Fig. 15 also shows that thermodynamic data overpredicts H$_2$ and CO$_2$ yields and underpredicts CO and CH$_4$ experimental compositions. Furthermore, Fig. 11 reports that synthesis gas composition obtained in the present study, is in closer agreement with the equilibrium compositions than the ones given by Salaices et al. [39,40]. One should also note that experiments were also conducted by varying the reaction time at 650 °C. These results are also included in Fig. 15. As can be seen, permanent gas compositions approach thermodynamic equilibrium compositions with the increase of reaction times from 5 to 30 s.

3.2.4. Effect of steam/biomass ratio

Fig. 16 reports dry gas yields and carbon conversions of glucose gasification at various steam/biomass ratios(S/B). It can be observed that an increase in the S/B ratio from 0.4 to 1.0 augments the dry gas yield as well as the carbon conversion. Thus, it appears that higher S/B ratios promote the steam reforming of hydrocarbons and water–gas shift reactions. For instance, when the S/B ratio is increased from 0.4 to 1.0 g/g, the dry gas yield augments from 8 to 10.4 mol/mol of glucose and the carbon conversion increases from 77.5 to 92%.

Fig. 17a–d reports the H$_2$, CO, CO$_2$ and CH$_4$ species compositions (dry basis) in the product gas using Cat A. Fig. 17a shows that
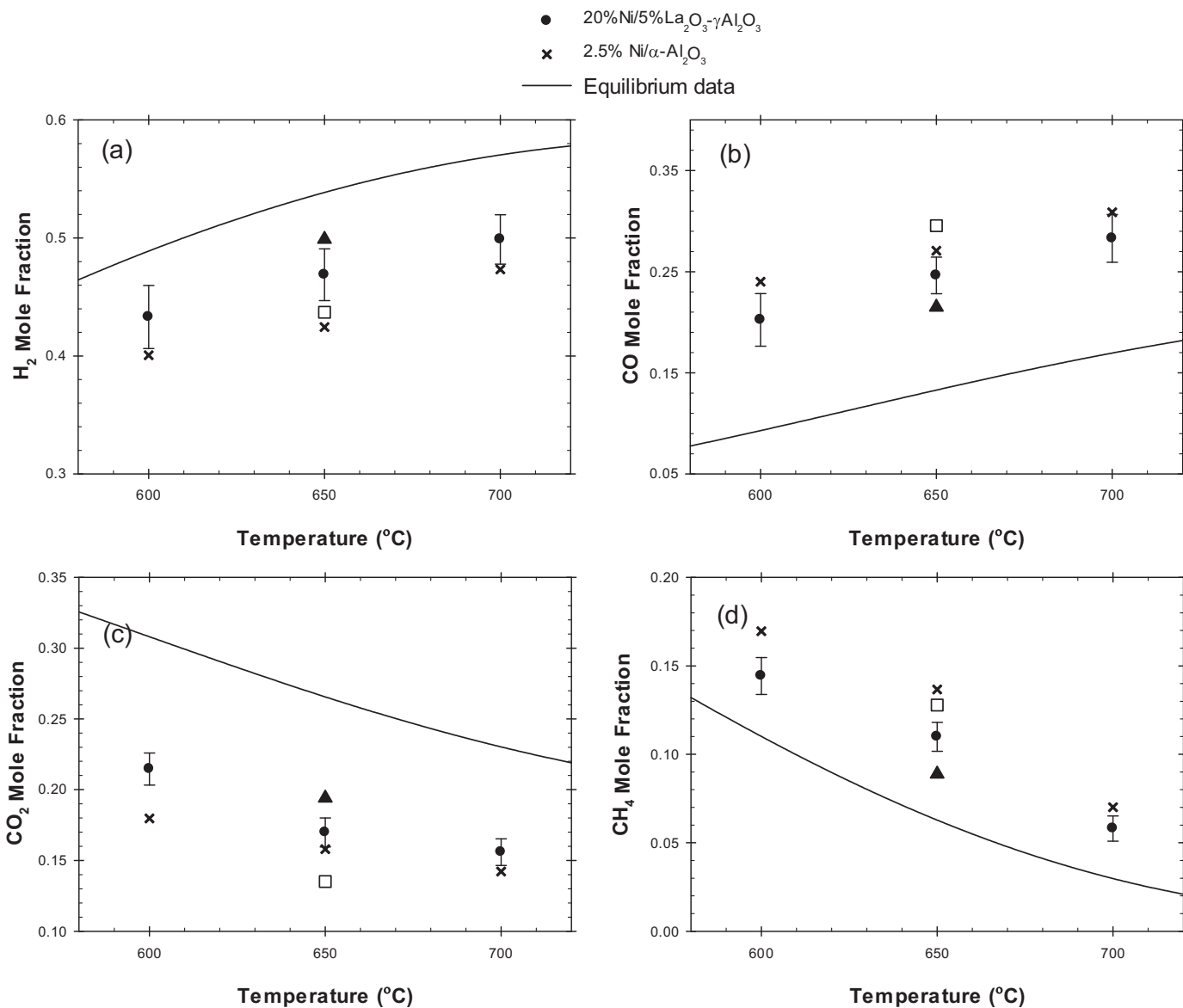
Fig. 15. Variation of product gas composition (dry basis) with temperature (a) H_2, (b) CO, (c) CO_2 and (d) CH_4, using Cat A (catalyst/biomass = 12.5) and $Ni/\alpha-Al_2O_3$ (catalyst/biomass = 25; data taken from Salaices et al. [39,40]). Lines represent the equilibrium data. Symbols □ and ▲ represent experimental data using Cat A for 5 and 30 s reaction time, respectively. [S/B ratio = 1.0 g/g; 20 s reaction time].
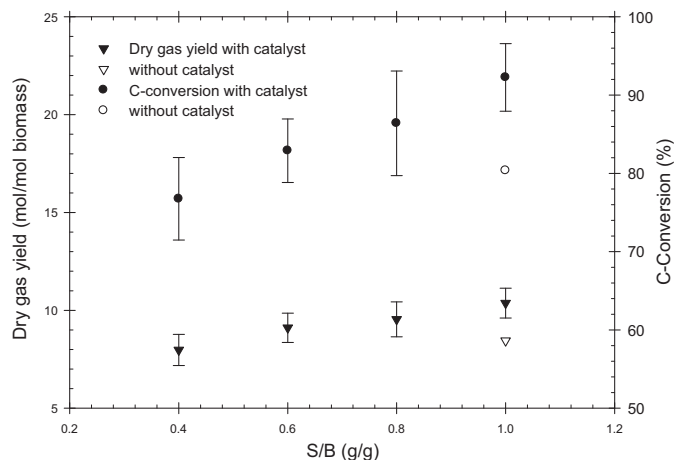

Fig. 16. Profiles of (a) dry gas yield and (b) carbon conversion with S/B during glucose gasification using Cat A and without a catalyst. [650 °C; catalyst/biomass = 8.75 to 12.5; 20 s reaction time].

higher S/B leads to an increased H_2 composition. This is a likely result of the higher extents of steam reforming, and homogeneous and heterogeneous water–gas shift reactions. Fig. 17b and c reports that CO_2 composition increases with S/B while CO concentration decreases. These trends can also be attributed to an increased influence of the water–gas shift reaction. Fig. 17d reports a decreasing CH_4 composition with the S/B. This behavior can be assigned to a more prevalent steam reforming reaction influence. One should also notice that the variations of H_2, CO, CO_2 and CH_4 compositions with S/B become milder at higher S/B s, as the reactions approach equilibrium.

Fig. 17 also reports equilibrium composition of H_2, CO, CO_2 and CH_4 in the product gas from glucose gasification at various S/B ratios. One can notice the close agreement of experimental species concentrations with the equilibrium reaction model predictions. In general, experimental H_2 and CO_2 compositions appear to be below thermodynamic predictions while CO and CH_4 compositions appear to be above thermodynamic predictions. The relatively short reaction time used in the CREC Riser Simulator gasifier
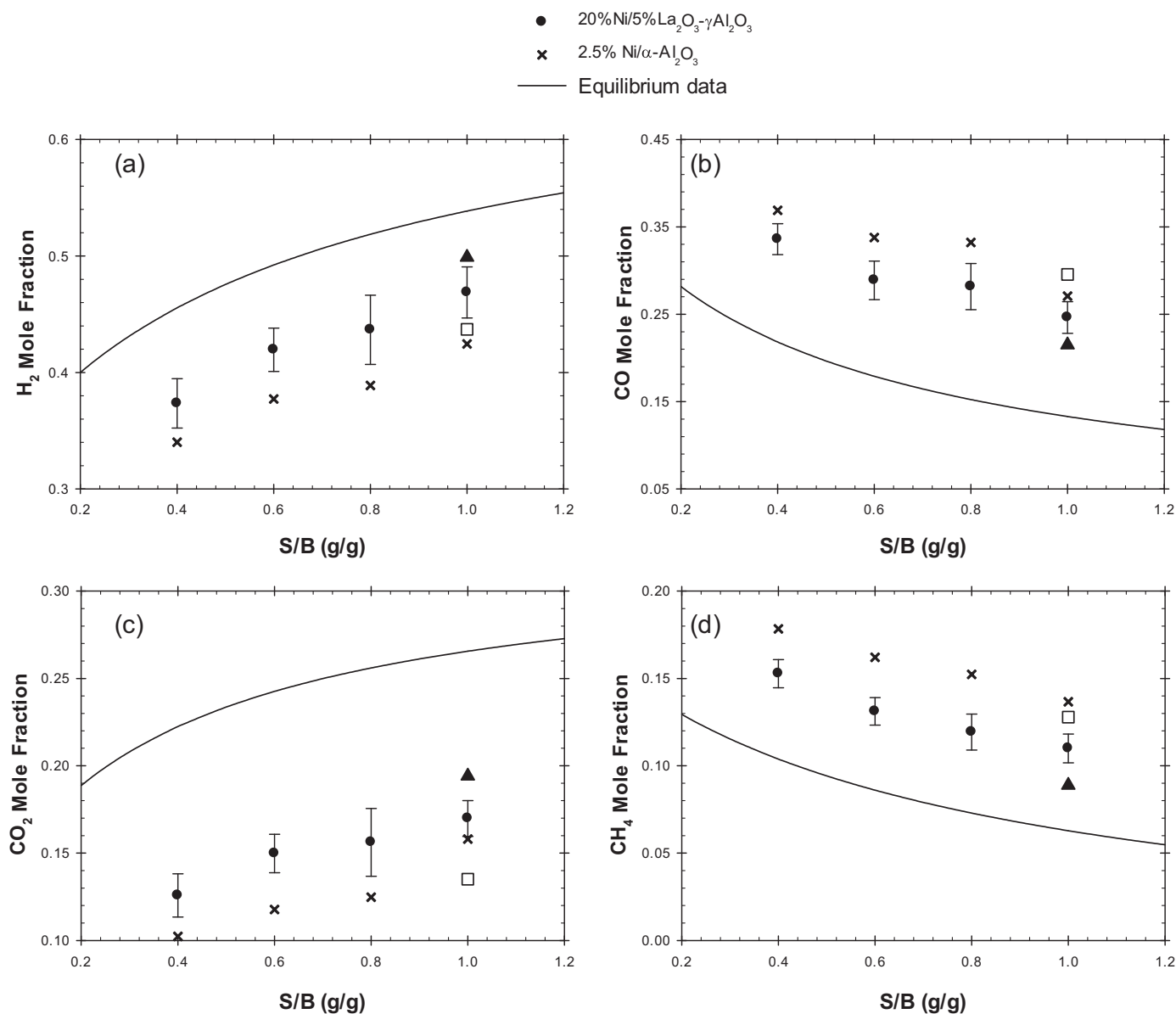
Fig. 17. Variation of product gas composition (dry basis) with S/B ratio (a) H_2, (b) CO, (c) CO_2 and (d) CH_4, using Cat A (catalyst/biomass = 8.75 to 12.5) and a Ni/α-Al$_2$O$_3$ catalyst(catalyst/biomass = 17.5 to 25); data taken from Salaices et al. [39,40]). Lines represent the equilibrium data. Symbols □ and ▲ represent experimental data using Cat A for 5 and 30 s reaction time, respectively. [650 °C; catalyst/biomass = 8.75 to 12.5; 20 s reaction time].

laboratory scale unit appears to be the reason for this difference between the experimental data and the thermodynamic predictions. In the specific case of a $S/B = 1.0$ g/g, experiments were conducted by varying reaction times as well. One can observe that increasing reaction times leads to gas compositions very close to those at reaction equilibrium.

A crucial parameter in biomass gasification is the H_2/CO ratio, which determines the quality of the syngas. Fig. 18 reports the H_2/CO ratios at the end of 20 s reaction time for various S/B ratios and temperatures. One can observe that increasing S/B, leads to a higher H_2/CO ratio. Thus, the higher steam partial pressure favors the water–gas shift reaction. One can also notice in Fig. 18 that the H_2/CO ratio increases from 1.1 to 1.9, when the S/B ratio is augmented from 0.4 to 1.0 g/g at 650 °C and at 20 s of reaction time. This H_2/CO ratio improvement tends, however, to be modest at higher S/B ratios. On the other hand, the H_2/CO ratio is reduced, when temperature is augmented (Fig. 14). The observed H_2/CO ratio decreases from 2.14 to 1.76 as the gasifier operation temperature is

raised from 600 to 700 °C at a $S/B = 1.0$ g/g and at 20 s reaction time. Once again, a reduced water–gas shift reaction (WGSR) influence at higher temperatures could be the reason behind this experimental finding.

3.2.5. Coke deposition

Coke deposited on the catalyst was measured after every gasification experiment by TOC analysis. Table 4 shows the average coke for four TOC experiments. The obtained results confirmed a small coke deposition on the catalyst surface with a maximum carbon-on-catalyst of 0.38 wt% at 20 s reaction time. Furthermore, a maximum of 7.86% of the carbon fed was found on the spent catalyst. However, coke deposition was decreased at higher temperatures and S/B ratios as these conditions favor coke reforming reactions.

One should mention that in some cases, catalysts were used for multiple gasification experiments (up to 15 cycles) with regeneration following every gasification runs. However, coke deposition

Table 4
TOC analysis of spent catalyst (Cat A).

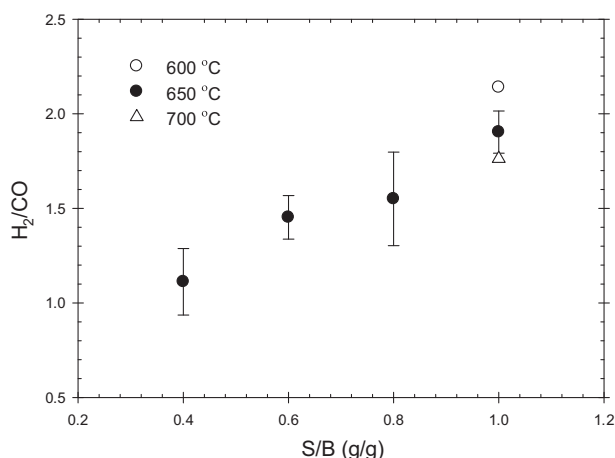| Temp (°C)	S/B ratio (g/g)	Reaction time (s)	Coke/catalyst (%)	Coke/C_{inj} (%)
600	1	20	0.16	5.06
650	1	20	0.14	4.43
700	1	20	0.12	3.82
	1	20	0.14	4.43
	0.8	20	0.19	5.28
	0.6	20	0.27	6.57
650	0.4	20	0.38	7.86
	1	5	0.20	6.24
	1	20	0.14	4.43
	1	30	0.10	3.30

Fig. 18. H_2/CO ratio of product gas from glucose gasification using Cat A at different S/B ratios (temperature = 650 °C) and at different temperatures (S/B = 1.0 g/g). [Catalyst/biomass = 8.75 to 12.5 g/g and 20 s reaction time].

remained close to the one obtained for single runs. One should notice, however, that after catalyst regeneration by air, the catalyst was re-reduced prior to the each gasification experiment as described in Section 2.3. This result demonstrates the regeneration-ability and stability of the prepared catalyst under repeated reaction/regeneration cycles.

Fig. 19 reports the diffraction patterns of the fresh and used (15 cycles of glucose gasification) Cat A. According to JCPDS 10-0425, the low intensity peaks centered at 2θ = 37.6°, 45.8° and 67.1° are the characteristic peaks of γ-Al_2O_3. Cat A also gives 2θ reflections of

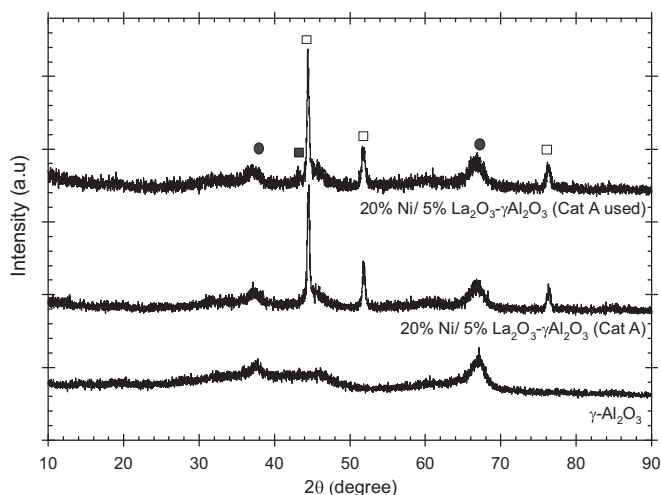**Fig. 19.** XRD patterns of the fresh and used Ni/La_2O_3-γAl_2O_3 catalyst (Cat A). (●: γ-Al_2O_3; □: Ni; ■: NiO).

Ni (JCPDS 04-850) centered at 2θ = 44.4°, 51.8° and 76.4°. As shown in Fig. 19, diffraction spectra of the fresh and used catalysts are almost the same expect the presence of a relatively small peak of NiO at 2θ = 43.3° in the used catalyst. For the purpose of comparison, crystallite sizes of Ni on the fresh and used catalysts were estimated by applying the Scherrer equation. The broadening of Ni (1 1 1) diffraction lines at 45.4°, gives essentially the same Ni crystallite size (27 nm) on the both fresh and used catalysts indicating negligible crystallite agglomeration. The diffraction pattern of the used catalyst also confirms the absence of graphitic coke formation.

4. Conclusions

A fluidizable Ni catalyst supported on La_2O_3 modified γ-Al_2O_3 has been developed for steam gasification of glucose (a cellulose surrogate of biomass) to produce high-quality and tar-free synthesis gas at temperatures below 700 °C. The following are the relevant conclusions of the present study:

(a) The addition of La_2O_3 up to 5 wt% helps to improve γ-alumina thermal stability, reducing thermal sintering. La_2O_3 also enhances the reducibility and dispersion of Ni/γ-Al_2O_3 catalysts by increasing the amount of easily reducible NiO species and inhibiting the formation of $NiAl_2O_4$.
(b) The introduction of La_2O_3 on the alumina support reduces Lewis acidity as well as increases the basicity of γ-Al_2O_3. This combined effect helps in inhibiting coke deposition.
(c) Significantly higher nickel reducibility and dispersion are obtained with the catalyst of present study employing direct reduction of metal nitrates instead of calcination in air.
(d) The prepared 20% Ni/5% La_2O_3-γAl_2O_3 catalyst showed stability under the repeated oxidation and reduction conditions of a gasification process. It consistently displayed 91.1% reducibility, 1.12% dispersion and a Ni crystal size of 87 nm.
(e) The gasification of glucose using the 20% Ni/5% La_2O_3-γAl_2O_3 catalyst gave significantly higher dry gas yields and carbon conversions. These yields were significantly closer to thermodynamic equilibrium versus the ones of a previous study [39,40] using a Ni/α-Al_2O_3 catalyst.
(f) The gasification of glucose with the catalyst of the present study yielded 95% carbon-conversion at temperatures as low as 700 °C with negligible coke deposition. Moreover, this catalyst also yielded a H_2/CO ratio close to 2.0 which makes the synthesis gas produced, a valuable feedstock for direct alcohol synthesis.

support with the diagrams as well as with the writing style of this manuscript.

References

[1] P. McKendry, Bioresour. Technol. 83 (2002) 55–63.
[2] A.V. Bridgwater, Chem. Eng. J 91 (2003) 87–102.
[3] L. Wang, C.L. Weller, D.D. Jones, M.a. Hanna, Biomass Bioenergy 32 (2008) 573–581.
[4] M. Balat, Energy Sources, A: Recover. Util. Environ. Eff. 31 (2009) 516–526.
[5] H.I. de Lasa, E. Salaices, J. Mazumder, R. Lucky, Chem. Rev. 111 (2011) 5404–5433.
[6] D. Sutton, B. Kelleher, J.R.H. Ross, Fuel Process. Technol. 73 (2001) 155–173.
[7] A.V. Bridgwater, Appl. Catal., A: Gen. 116 (1994) 5–47.
[8] J. Han, H. Kim, Renewable Sustainable Energy Rev. 12 (2008) 397–416.
[9] S. Nanda, P. Mohanty, K.K. Pant, S. Naik, J.a. Kozinski, A.K. Dalai, Bioenergy Res. 6 (2012) 663–677.
[10] L. Garcia, A. Benedicto, E. Romeo, M.L. Salvador, J. Arauzo, R. Bilbao, Energy Fuels 16 (2002) 1222–1230.
[11] E. Gusta, A.K. Dalai, M.A. Uddin, E. Sasaoka, Energy Fuels 23 (2009) 2264–2272.
[12] Z. Abu El-Rub, E.A. Bramer, G. Brem, Ind. Eng. Chem. Res. 43 (2004) 6911–6919.
[13] L. Devi, K.J. Ptasinski, F.J.J.G. Janssen, Biomass Bioenergy 24 (2003) 125–140.
[14] E.G. Baker, L.K. Mudge, M.D. Brown, Ind. Eng. Chem. Res. 26 (1987) 1335–1339.
[15] J. Ashok, S. Kawi, Int. J. Hydrogen Energy 38 (2013) 13938–13949.
[16] P. Lan, Q.-L. Xu, L.-H. Lan, D. Xie, S.-P. Zhang, Y.-J. Yan, Energy Sources, A: Recover. Util. Environ. Eff. 34 (2012) 2004–2015.
[17] L. Garcia, R. French, S. Czernik, E. Chornet, Appl. Catal., A: Gen. 201 (2000) 225–239.
[18] R. Martínez, E. Romeo, L. García, R. Bilbao, Fuel Process. Technol. 85 (2003) 201–214.
[19] K. Tomishige, T. Kimura, J. Nishikawa, T. Miyazawa, K. Kunimori, Catal. Commun. 8 (2007) 1074–1079.
[20] A. Iriondo, V.L. Barrio, J.F. Cambra, P.L. Arias, M.B. Güemez, R.M. Navarro, M.C. Sanchez-Sanchez, J.L.G. Fierro, Catal. Commun. 10 (2009) 1275–1278.
[21] H. Schaper, E.B.M. Doesburg, L.L. van Reijen, Appl. Catal. 7 (1983) 211–220.
[22] H. Schaper, E.B.M. Doesburg, P.H.M. de Korte, L.L. van Reijen, Solid State Ionics 16 (1985) 261–265.
[23] M.M. Hossain, D. Lopez, J. Herrera, H.I. de Lasa, Catal. Today 143 (2009) 179–186.
[24] M. Sanchez-Sanchez, R. Navarro, J. Fierro, Catal. Today 129 (2007) 336–345.
[25] S. Bona, P. Guillen, J. Alcalde, L. Garcia, R. Bilbao, Chem. Eng. J. 137 (2008) 587–597.
[26] Z.-W. Liu, H.-S. Roh, K.-W. Jun, J. Ind. Eng. Chem. 9 (2003) 267–274.
[27] Y. Jilei, L. Zengxi, D. Huachao, L. Yuan, J. Rare Earths 24 (2006) 302–308.
[28] Y. Cui, H. Zhang, H. Xu, W. Li, Appl. Catal., A: Gen. 331 (2007) 60–69.
[29] P. Kumar, Y. Sun, R.O. Idem, Energy Fuels 22 (2008) 3575–3582.
[30] B. Valle, A. Remiro, A.T. Aguayo, J. Bilbao, A.G. Gayubo, Int. J. Hydrogen Energy 38 (2013) 1307–1318.
[31] C.H. Bartholomew, R.J. Farrauto, J. Catal. 45 (1976) 41–53.
[32] Y.-J. Huang, J.A. Schwarz, Appl. Catal. 30 (1987) 255–263.
[33] Y. Kim, C. Kim, P. Kim, J. Yi, J. Non-Cryst. Solids 351 (2005) 550–556.
[34] J.M. Ginsburg, J. Pin, T. El Solh, H.I. de Lasa, Ind. Eng. Chem. Res. 44 (2005) 4846–4854.
[35] J. Ginsburg, H.I. de Lasa, Int. J. Chem. Reactor Eng. 3 (2005) 1–18.
[36] K. Jarosch, H.I. de Lasa, Chem. Eng. Sci. 54 (1999) 1455–1460.
[37] T. El Solh, K. Jarosch, H.I. de Lasa, Appl. Catal., A: Gen. 210 (2001) 315–324.
[38] T. El Solh, K. Jarosch, H.I. de Lasa, Ind. Eng. Chem. Res. 42 (2003) 2507–2515.
[39] E. Salaices, B. Serrano, H.I. de Lasa, Ind. Eng. Chem. Res. 49 (2010) 6834–6844.
[40] E. Salaices, Catalytic steam gasification of biomass surrogates: a thermodynamic and kinetic approach, in: Ph.D. Thesis, The University of Western Ontario, London, ON, Canada, 2010.
[41] H.I. de Lasa, Riser simulator, in: US Patent 5102628, 1992.
[42] M.C. Alvarez-Galvan, R.M. Navarro, F. Rosa, Y. Briceño, F.G. Alvarez, J.L.G. Fierro, Int. J. Hydrogen Energy 33 (2008) 652–663.
[43] R.M. Navarro, M.C. Álvarez-Galván, F. Rosa, J.L.G. Fierro, Appl. Catal., A: Gen 297 (2006) 60–72.
[44] E.P. Parry, J. Catal. 2 (1963) 371–379.
[45] C. Morterra, G. Magnacca, Catal. Today 27 (1996) 497–532.
[46] A.A. Khaleel, K.J. Klabunde, Chem. Eur. J. 8 (2002) 3991–3998.
[47] V. La Parola, G. Deganello, S. Scirè, A.M. Venezia, J. Solid State Chem. 174 (2003) 482–488.
[48] C. Morterra, S. Coluccia, A. Chiorino, F. Boccuzzi, J. Catal. 54 (1978) 348–364.
[49] C. Morterra, A. Chiorino, G. Ghiotti, E. Garrone, J. Chem. Soc., Faraday Trans. 1: Phys. Chem. Condens. Phases 75 (1979) 271–288.
[50] X. Liu, R.E. Truitt, J. Am. Chem. Soc. 119 (1997) 9856–9860.
[51] C. Morterra, A. Zecchina, S. Coluccia, A. Chiorino, J. Chem. Soc., Faraday Trans. 1: Phys. Chem. Condens. Phases 73 (1977) 1544–1560.
[52] C. Choong, L. Huanga, Z. Zhonga, J. Lina, L. Hong, L. Chen, Appl. Catal., A: Gen. 407 (2011) 155–162.
[53] V. Guggilla, J. Akyurtlu, A. Akyurtlu, I. Blankson, Ind. Eng. Chem. Res. 49 (2010) 8164–8173.
[54] W. Gac, Appl. Surf. Sci. 257 (2011) 2875–2880.
[55] G. Xu, K. Shi, Y. Gao, H. Xu, Y. Wei, J. Mol. Catal. A: Chem. 147 (1999) 47–54.
[56] H. Liu, D. He, Int. J. Hydrogen Energy 36 (2011) 14447–14454.
[57] M. Sanchez-Sanchez, R. Navarro, J. Fierro, Int. J. Hydrogen Energy 32 (2007) 1462–1471.
[58] M.M. Hossain, H.I. de Lasa, AIChE J. 53 (2007) 1817–1829.
[59] T. Horiuchi, H. Hidaka, T. Fukui, Y. Kubo, M. Horio, K. Suzuki, T. Mori, Appl. Catal., A: Gen. 167 (1998) 195–202.